




All-dielectric six-foci metalens for infrared polarization detection based on Stokes space

ENZHU HOU,¹ ZHONGZHU LIANG,^{1,2,*} XIAOYAN SHI,¹ FUMING YANG,^{1,2} YONGJUN DONG,¹ ZHE WU,¹ RUI DAI,¹ HUA LIU,¹  AND SIXUAN LI¹

¹Center for Advanced Optoelectronic Functional Materials Research and Key Laboratory of UV Light-Emitting Materials and Technology of Ministry of Education, College of Physics, Northeast Normal University, Changchun 130024, China

²Changchun Institute of Optics, Fine Mechanics and Physics, Chinese Academy of Sciences, Changchun, Jilin, 130033, China

*liangzz@nenu.edu.cn

Abstract: The detection technology of infrared polarization has gained significant attention due to its ability to provide better identification and obtain more information about the target. In this paper, based on the expression of the full polarization state in Stokes space, we designed micro-nano metasurface functional arrays to calculate the polarization state of the incident light by reading the Stokes parameters (a set of parameters that describe the polarization state). Metalens with linear and circular polarization-dependent functions are designed based on the propagation and geometric phases of the dielectric Si meta-atoms in the infrared band, respectively. The device exhibits a high polarization extinction ratio. The influence of incident angle on polarization-dependent metalens is discussed, and the analysis of incident angle is of great significance for the practical application. An infrared six-foci metalens is proposed, each corresponding to the Poincaré sphere's coordinate component (a graphical polarization state method). By matching the six polarization components of the incident light and the Stokes parameters, the polarization detection function can be realized by calculating the polarization state of the incident light. There is a slight error between the theoretical value and the calculated value of the unit coordinate component of the Stokes parameters. At the same time, the intensity distribution of different incident light polarization azimuth angles and ellipticity angles on the focal plane agrees with the theory. The advantage of the device is that the polarization state of the incident light can be directly calculated without passing through other components. The six-foci metalens have potential applications in polarization detection and imaging, space remote sensing, etc.

© 2023 Optica Publishing Group under the terms of the [Optica Open Access Publishing Agreement](#)

1. Introduction

Polarization is an inherent characteristic of electromagnetic waves, which contains abundant information and is significant in sensing [1,2], detection [3–6], and recognition [7–9]. Polarization detection of visible light has matured significantly, primarily due to band considerations. However, susceptibility to environmental factors is a disadvantage of visual light detection. And both military and civilian facilities emit infrared radiation as a common occurrence. Recently, there has been an increasing interest in using infrared polarization detection technology [10–12]. Polarization detection is more effective for identifying targets and providing additional information, such as azimuth angle and ellipticity angle [13,14] than traditional intensity detection methods. Polarization measurement-based devices and technologies face the challenge of a restricted field of view, and their systems are often intricate. When measuring the polarization state, it's necessary to use beam splitters, waveplates, and polarizers in combination. The size and

complexity of systems tend to grow larger, which goes against the trend of developing compact and integrated devices [15–19].

As an ultra-thin artificial material composed of two-dimensional (2D) subwavelength micro-nano structure arrays, metasurfaces have been proven to be a compact and effective platform for modifying light amplitude [20,21], phase [22–24] and polarization [20,25]. They are significant in the future of device miniaturization and integrated development. In 2011, Cappa et al. proposed the generalized Snell's law, which shows that the separated subwavelength optical resonators can produce a phase mutation when the propagation light passes through the interface between the two media [26]. Since then, phase-controlled metasurfaces have gained widespread attention. Recently, the application of metasurfaces in functional metalens [27–29], vortex beam generation [30,31], Multi-channel holographic imaging [32–36], and optical neural network devices [8,37–40] have been impressive, promoting the development of digital optics and computational optics [40]. Due to the flexibility of multi-parameter modulation, each meta-atom can be designed to manipulate multiple properties of light simultaneously [20,41,42], and it is also considered a preferred candidate for polarization manipulation. The relevant research on metasurface polarization detection is mainly achieved by combining traditional devices such as polarization metasurfaces and polarizers or by the rotation of metasurface polarizing devices [4,7,35]. Therefore, it is only feasible to detect polarization characteristics at a time, and making conventional instruments is still necessary.

In this paper, we proposed a full polarization detection of infrared six-foci metalens based on Stokes space, with focal spots corresponding to the six polarization components of the detected incident light (corresponding to the coordinate components of the Poincaré sphere). The polarization state of the incident light can be calculated from the intensity of the six polarization components in the focal plane. Infrared linear and circular polarization-dependent metalens are designed with a high polarization extinction ratio based on propagation and geometric phases. The influence of incident angle on the focal plane intensity distribution and focus position of polarization-dependent metalens was analyzed. The proposed six-foci metalens extract the Stokes parameter through the focal plane, and the polarization state of the incident light can be inverted by calculation. The intensity distribution of polarization azimuth and ellipticity angles of different incident lights in the focal plane was analyzed. The error between the theoretical and calculated values of the unit Stokes coordinate parameters is small, which is of great significance for polarization detection and imaging.

2. Principle and design

2.1. Linear polarization metalens

The designed meta-atom structure must meet polarization selection conditions to realize the linear polarization-dependent metasurface devices accompanied by a high extinction ratio. The schematic diagram of the rectangular Si column meta-atom structure is shown in Fig. 1(a), and its height is $H = 6.5\mu\text{m}$. Here, the linear polarization (LP) characteristics are designed based on the propagation phase, and the characteristic dimensions of the rectangular Si column are parametrically analyzed. Figure 1(c) and 1(d) show the phase and transmission at $10.6\mu\text{m}$ of Si meta-atom structures with different lengths L and widths D , in which eight meta-atom structures are selected. A phase gradient of 2π satisfies the x-direction with high transmission, and a relatively stable phase in the y-direction is achieved, as shown in Fig. 1(b). Each meta-atom structure can be equated to a birefringence element, and the structure group can be used to implement linear polarization-dependent functional modulation devices. The metalens is designed based on the finite-difference time-domain (FDTD) method. Periodic boundary conditions were applied in both the x and y directions, while the perfectly matched-layer (PML) boundary condition was applied in the z direction (light wave propagation).

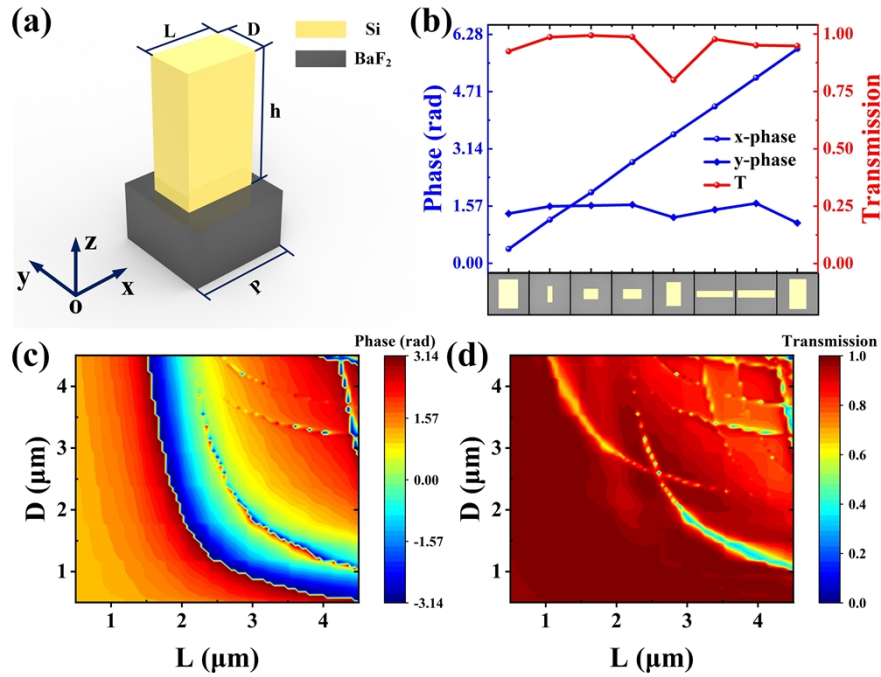


Fig. 1. (a) Schematic diagram of the phase-control meta-atom structure; (b) phase and transmission of the selected meta-atom structure (corresponding structure size: $L_1 = 2.4\mu\text{m}$ and $D_1 = 3.6\mu\text{m}$, $L_2 = 0.6\mu\text{m}$ and $D_2 = 2\mu\text{m}$, $L_3 = 1.8\mu\text{m}$ and $D_3 = 1.3\mu\text{m}$, $L_4 = 2.3\mu\text{m}$ and $D_4 = 1.2\mu\text{m}$, $L_5 = 1.8\mu\text{m}$ and $D_5 = 2.95\mu\text{m}$, $L_6 = 4.5\mu\text{m}$ and $D_6 = 0.77\mu\text{m}$; $L_7 = 4.5\mu\text{m}$ and $D_7 = 0.9\mu\text{m}$ and $L_8 = 2.1\mu\text{m}$ and $D_8 = 3.7\mu\text{m}$); the (c) phase and (d) transmission at $10.6\mu\text{m}$ corresponding to size L and D.

The schematic of linear polarization-dependent metalens is shown in Fig. 2(a). The horizontal linear polarization (HLP) light is focused on one spot through metalens, and the vertical linear polarization (VLP) light is close to plane wave emission without a focal spot. This is also why when we select the element structure, the phase in the x direction meets the phase adjustment conditions, and the phase in the y direction needs to be selected as the stabilization. The system consists of a BaF₂ [43] substrate with a relatively low refractive index and a subwavelength rectangular Si [44] column with a relatively high refractive index. The required phase distribution of the metalens can be described as the following Eq. (1) [45–47]:

$$\varphi = -\frac{2\pi}{\lambda}(\sqrt{r^2 + f^2} - f) \quad (1)$$

where λ and f are design wavelength and focal length, respectively, and x and y are the coordinates position in the metalens. Under intensity-normalized conditions, the intensity distribution of HLP metalens under the incidence of HLP light and VLP light is shown in Fig. 2(b). There is a focal spot at the center of the x - y plane and the x - z plane $z = 80\mu\text{m}$ in incident HLP light. However, there is almost no light field distribution in incident VLP light, indicating near-plane wave propagation. At the same time, we analyzed the intensity of the light field at $y = 0$ in the x - y focal plane, as shown in Fig. 2(c). It can be seen from the figure that the metalens exhibit an extremely high extinction ratio and a full width at half maximum (FWHM) of $6.19\mu\text{m}$.

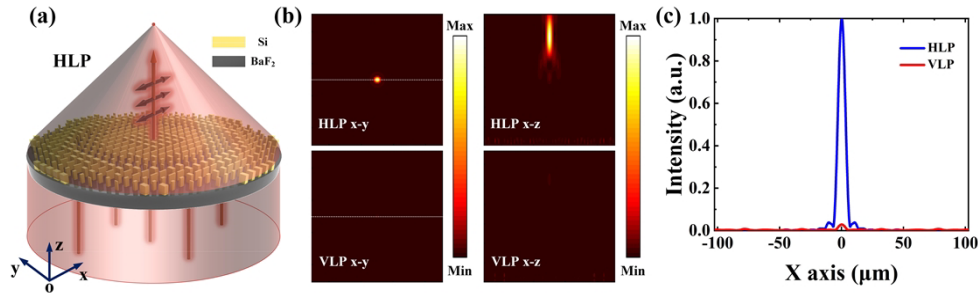


Fig. 2. (a) Schematic diagram of linear polarization-dependent metalens; (b) the intensity distribution in the x - y focal plane and x - z plane, in the case of horizontal linear polarization (polarized along the x -axis, HLP) light and vertical linear polarization (polarized along the y -axis, VLP) light incidence; (c) Comparison of the normalized intensity distribution of HLP light and VLP light at $y = 0$ in the focal plane.

2.2. Circular polarization metalens

The geometric phase is the best choice for phase control of circular polarization (CP) light wavefront [22,23,48,49]. In the case of the CP light incidence $\sqrt{2}/2(1, \pm i)^T$, the Jones vector of output light E_{out} can be expressed as the following [49]:

$$E_{\text{out}} = \frac{\sqrt{2}}{2} \cos \frac{\Gamma}{2} \begin{pmatrix} 1 \\ \pm i \end{pmatrix} - i \frac{\sqrt{2}}{2} \sin \frac{\Gamma}{2} e^{2\theta i} \begin{pmatrix} 1 \\ \mp i \end{pmatrix} \quad (2)$$

Γ is the phase delay in the x and y directions, and θ is the rotation angle of the meta-atom (defined as the angle between the long axis and the x -axis of the meta-atom). Therefore, to achieve high conversion efficiency for the geometric phase meta-atom structure, two conditions need to be met: the high transmission of the electric field and the phase delay of the π between the quadrature electric field components, which can be equivalent to a half-waveplate.

The designed meta-atom structure is shown in Fig. 3(a), the rectangular Si column: $L = 3.5\mu\text{m}$, $D = 1.1\mu\text{m}$, $H = 6.5\mu\text{m}$. Under the condition of left-handed (or right-handed) polarized light incidence, with the change of the rotation angle θ of the meta-atom, the phase change of the right-handed (or left-handed) outgoing light satisfies the phase $\varphi = 2\theta$, accompanied by a relatively high transmission. To reveal the mechanism of π phase delay, we studied the electric and magnetic fields in the optimal meta-atom, shown in Fig. 3(c) and 3(d). As shown in the electric field distribution of Fig. 3(c), it can be seen that the induced electric field contains two ring currents with alternating clockwise and counterclockwise directions, which correspond to two (even-numbered) antiparallel magnetic dipoles (AMD) [50] positioned vertically along the z -axis. For the E_x component, the electrical vectors' direction at the incident (bottom) and output (top) ends of the rectangular Si column are oriented in the same direction, and the x component of the CP light is held after passing through the meta-atom. However, for the E_y component, the induced electric field excites one (odd-numbered) AMD and the odd-numbered circular displacement currents such that the electric vector of the transmitted light is opposite to the electrical vector of the incident light, shown in Fig. 3(d), revealing the phase delay π . Therefore, the transmitted light exhibits polarization that is entirely orthogonal to the incident light and exhibits high-efficiency polarization conversion. From the above analysis, it can also be seen that the number of modes that the rectangular Si column structure can accommodate in the x and y directions is related to the wavelength. At the same time, it can also be shown that the metasurface element structure that meets the conditions is not unique.

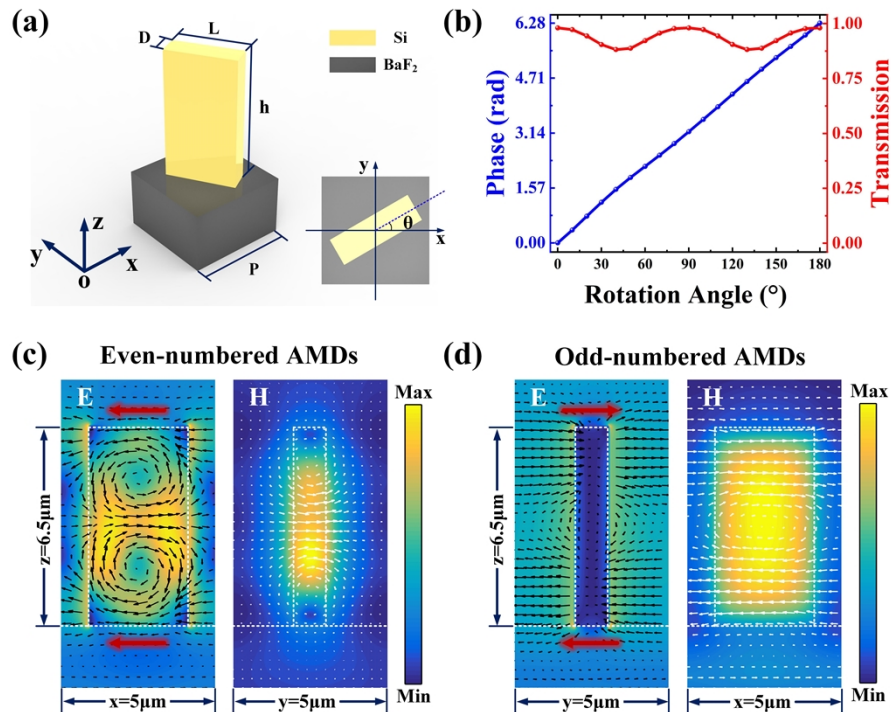


Fig. 3. (a) Schematic diagram of the geometric phase meta-atom structure; (b) phase and transmission of different rotation angle meta-atom structures at $10.6\ \mu\text{m}$; The total electric field (E) and magnetic field (H) present in the geometric phase meta-atom structure when the incident light of (c) x polarization and (d) y polarization are excited.

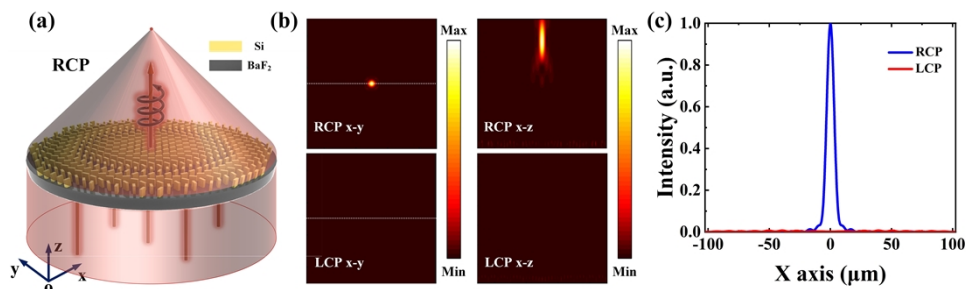


Fig. 4. (a) Schematic diagram of a circular polarization-dependent metasurface; (b) the intensity distribution in the x-y focal plane and the x-z plane, in the case of left-handed circular polarization (LCP) light and right-handed circular polarization (RCP) light incidence; (c) Comparison of the normalized intensity distribution of LCP light and RCP light at $y = 0$ in the focal plane.

Figure 4(a) shows a schematic diagram of a circular polarization-dependent focused metalens. The incident RCP light is converted into the LCP light converging at the focal spot through the metalens array. The metalens is also based on BaF₂ and consists of rectangular Si column structures with different rotation angles. The phase distribution is the same as Eq. (1), and the focal length f of the device is 80 μm . Figure 4(b) shows the intensity distribution of the designed metalens in the case of LCP light and RCP light incidence. There is a focal spot at the center of the x - y plane and the x - z plane $z = 80 \mu\text{m}$ in incident RCP light. However, due to the rotation direction of the geometric phase meta-atom being associated with the rotation direction of the incident CP light, there is no focus on the incidence of the LCP light. The intensity at the focal plane $y = 0$ is normalized and analyzed, as shown in Fig. 4(c). It can be seen from Fig. 4(c) that the CP metalens also has a high extinction ratio and an FWHM of 7.08 μm .

2.3. Influence of incidence angles

The angle modulation characteristics of the HLP and RCP metalens are further analyzed to discuss the influence of incident angle on the above two devices, as shown in Fig. 5. As the incident angle changes from 0 to 20°, the focal spots of the two metalens in the focal plane shift significantly along the y -axis, and the larger the incident angle, the greater the focal spot offset in the focal plane. The basis on which metasurfaces can achieve wavefronts is the generalized Snell's law, expressed as follows:

$$\sin(\theta_t) - \sin(\theta_i) = \frac{\lambda}{2\pi} \frac{\partial \varphi}{\partial r} \quad (3)$$

where θ_t is the transmission angle, and θ_i is the angle of incidence. Combined with the wavefront phase distribution formula of the metalens:

$$\sin(\theta_t) = -\frac{r}{\sqrt{f^2 + r^2}} + \sin(\theta_i). \quad (4)$$

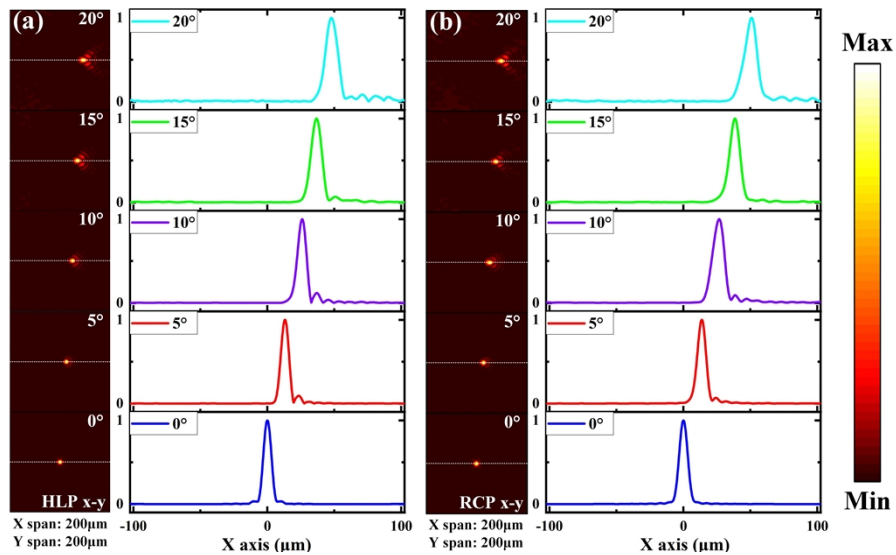


Fig. 5. The influence of incidence angles of 0°, 5°, 10°, 15°, and 20° on (a) the HLP and (b) the RCP metalens, focal plane intensity, and normalized intensity at the dashed line.

According to the ray tracing of geometric optics, the approximate change trend of the focal point can be obtained. As the angle of incidence increases, the transmitted light from a metalens

cannot be perfectly focused. However, the angle of incidence is within a specific range, and the focus can still be focused on the focal plane. When the incident light is oblique, the focus of the metasurface is related to the array size, focal length, and incident angle. Table 1 outlines the changes in the y-axis offset, output angle, and the FWHM due to variations in the incident angle. It can be seen from the data that as the incident angle increases, the y-axis offset increment becomes smaller. The focus offsets of HLP and RCP light are similar for the same incident angle conditions. Meanwhile, the FWHM tends to widen, except for the RCP light at an incident angle of 10°.

Table 1. Data statistics: angle of incidence causes a change

Polarization state	Incident angle (Deg)	Focus offset (μm)	Output angle (Deg)	FWHM (μm)
HLP light	0	0	0	6.19
	5	13.32	9.45	6.94
	10	26.01	18.01	7.68
	15	36.85	24.73	9.41
	20	47.69	30.80	10.71
RCP light	0	0	0	7.08
	5	13.63	9.87	7.48
	10	26.63	18.41	10.18
	15	38.40	25.64	9.13
	20	50.79	32.42	10.73

3. Infrared six-foci metalens for polarization detection

In 1852, Stokes proposed four parameters to represent the intensity and polarization state of light waves, a schematic diagram shown in Fig. 6(a). In characterizing polarization states, the Stokes vector method can express arbitrary polarization states and be easily detected. Therefore, it has been widely used in polarization detection. The Stokes parameters are described as follows [41,51]:

$$S = \begin{pmatrix} S_0 \\ S_1 \\ S_2 \\ S_3 \end{pmatrix} = \begin{pmatrix} I_X + I_Y \\ I_X - I_Y \\ I_{45^\circ} - I_{-45^\circ} \\ I_{RCP} - I_{LCP} \end{pmatrix} = S_0 \begin{pmatrix} 1 \\ \cos 2\psi \cos 2\chi \\ \sin 2\psi \cos 2\chi \\ \sin 2\chi \end{pmatrix}, \quad (5)$$

where ψ is the azimuth angle, and χ is the ellipticity angle, shown in Fig. 6(b) in the schematic diagram of the vibration trajectory. We designed a six-foci polarization metalens device based on Stokes space coordinates to enable polarization detection. Figure 6(c) shows a schematic diagram of the designed six-foci metalens for polarization detection. The polarization-dependent metalens intensity information extracts the Stokes parameter of incident light on the Poincaré sphere. The polarization state of the incident light is calculated in reverse by the extracted Stokes parameter.

We further calculated and analyzed the polarization detection capability of a six-foci metalens device. Stokes parameters for incident light can be calculated by passing through the intensity information, as shown in Eq. (5). Therefore, the device can measure the polarization state of the incident light at once. The focus corresponds to the Stokes parameters as follows: HLP and VLP correspond to S_1 and $-S_1$, respectively; LP_{45° and LP_{-45° correspond to S_2 and $-S_2$, respectively; and RCP and LCP correspond to S_3 and $-S_3$, respectively. The focal plane intensity

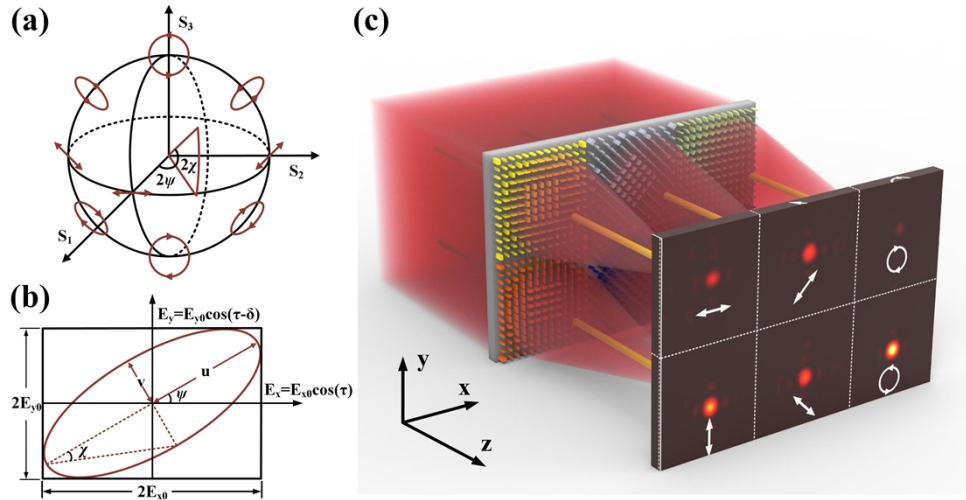


Fig. 6. Schematic diagram of (a) the Poincaré sphere, (b) the polarization vibration trajectories, and (c) the six-foci infrared polarization detection.

distribution of the incident polarization light with different azimuth angles is shown in Fig. 7(a). The LCP and RCP components have little effect as the azimuth angle increases. In the case of the LP light incidence, the LCP and RCP intensities are theoretically equal. According to the components of the incident LP light in the x , y , 45° , and -45° directions, the conclusions in the above Fig. 7(a) are consistent with the theoretical laws. Then, the detection results of different ellipticity angles are analyzed in the focal plane, as shown in Fig. 7(b). From the figure, it is possible to ascertain whether the incident light is left-handed or right-handed; the left-handed light incidence is focused more intensity of the left-handed component, as shown in the first four figures; conversely, the right-handed light incidence is focused more intensity of the right-handed component, shown in the last four figures. Overall, each incident polarization state generates a unique intensity distribution, indicating that the six-foci metalens exhibit high polarization-dependent characteristics.

The azimuth angle and ellipticity angle of the polarization trajectory can be further calculated by the Stokes parameter corresponding to Eq. (5) and are as follows:

$$\chi = \frac{\arcsin(S_3)}{2}, \quad \psi = \frac{\arctan(S_2/S_1)}{2}. \quad (6)$$

The Stokes coordinate parameters were normalized, as shown in Table 2. The calculated and theoretical values of the device show a good match with a small error (the error equation is shown in Eq. (7)).

$$S_{error} = \sqrt{(S_1' - S_1)^2 + (S_2' - S_2)^2 + (S_3' - S_3)^2} / 3 \times 100\%. \quad (7)$$

One of the factors that can cause errors is the selection of the structure of the linear polarization element. Considering the experimental accuracy, the designed linear polarization element structure satisfies eight phase gradients in the x direction and phases similar but not identical in the y direction. In the focused Fig. 2(c), it can be seen that although there is a high polarization extinction ratio, there is an energy distribution in the focal plane when the incident of polarized light in the y direction is incident. Another factor is the interaction between arrays, which affects the independence of Stokes parameter extraction. In the future, optimization can be carried out in the following three directions: Design the linear polarizing element structure in the y direction to be as equal as possible; Establish independent optical information channels to reduce mutual

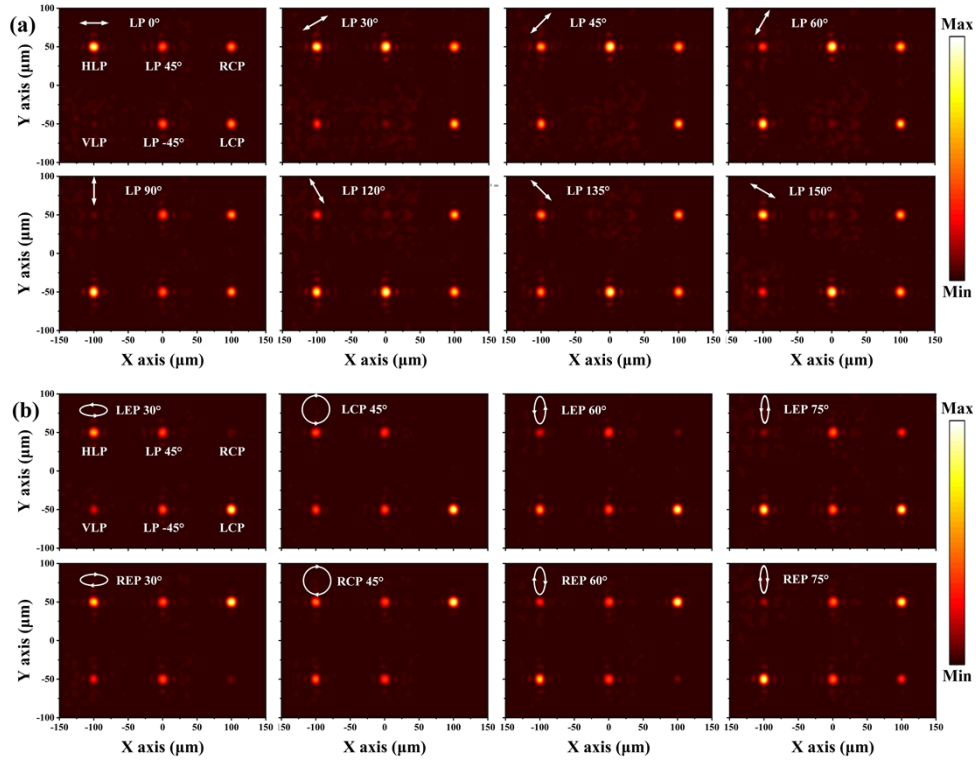


Fig. 7. Focal plane intensity distribution of (a) different azimuth angles and (b) different ellipticity angles.

Table 2. Stokes parameter analysis of infrared six-foci metalens

Polarization state	Theoretical Values (S_1, S_2, S_3)			Calculated Values (S_1', S_2', S_3')			Error (%)
HLP	1	0	0	0.9781	0.1625	0.1301	6.9
VLP	-1	0	0	-0.9890	-0.0678	0.1312	4.9
LP45°	0	1	0	-0.1665	0.9842	0.0601	5.9
LP-45°	0	-1	0	0.0490	-0.9955	0.0805	3.1
RCP	0	0	1	-0.0106	-0.0053	0.9999	0.03
LCP	0	0	-1	-0.0320	0.0215	-0.9993	1.2

interference between different polarization modules; Through the later data processing module, the corresponding data optimization is carried out to improve the accuracy. At the same time, according to the device's material, size, and aspect ratio, the device is manufactured by the electron beam lithography process method.

4. Conclusion

In conclusion, the infrared six-foci metalens was proposed based on the Stokes parameter for infrared polarization detection. The intensity of the focal plane corresponds to the three coordinate components (including plus and minus) of Stokes Space. Based on the propagation and geometric phases, linear and circular polarization-dependent metalens were designed, respectively, with the FWHM of $6.19 \mu\text{m}$ and $7.08 \mu\text{m}$. The influence of incident angle on the LP and CP metalens is

discussed and analyzed. Stokes Parameter was matched using linearly polarization and circular polarization-dependent metalenses to form a 6-focus metalens for infrared polarization detection. The polarization state of the incident light is obtained by calculating the Stokes parameters to achieve the function of polarization detection. The focal plane intensity distribution of different azimuth and ellipticity angles in the polarization trajectory was analyzed. The theoretical and calculated values of the unit coordinates of Stokes space are compared, showing a slight error and giving some optimization directions. Therefore, the above conclusions show that the device significantly applies polarization detection, imaging, and space remote sensing in the infrared band.

Funding. Distinguished Young Scholars of Jilin Province (20230101351JC); Scientific and Technological Development Project of Jilin Province (20220201080GX); National Natural Science Foundation of China (61735018); Excellent Member of Youth Innovation Promotion Association of the Chinese Academy of Sciences (Y201836); Leading Talents and Team Project of Scientific and Technological Innovation for Young and Middle-aged Groups in Jilin Province (20190101012JH).

Disclosures. The authors declare no conflicts of interest.

Data availability. Data underlying the results presented in this paper are available in Ref. [43] and [44].

References

1. M. Dai, C. Wang, B. Qiang, *et al.*, “Long-wave infrared photothermoelectric detectors with ultrahigh polarization sensitivity,” *Nat. Commun.* **14**(1), 3421 (2023).
2. B. Chen, Z. Ji, J. Zhou, *et al.*, “Highly polarization-sensitive far infrared detector based on an optical antenna integrated aligned carbon nanotube film,” *Nanoscale* **12**(22), 11808–11817 (2020).
3. M. Oshita, S. Saito, and T. Kan, “Electromechanically reconfigurable plasmonic photodetector with a distinct shift in resonant wavelength,” *Microsyst. Nanoeng.* **9**(1), 26 (2023).
4. R. Wang, J. Han, J. Liu, *et al.*, “Multi-foci metalens for terahertz polarization detection,” *Opt. Lett.* **45**(13), 3506–3509 (2020).
5. J. Wei, C. Xu, B. Dong, *et al.*, “Mid-infrared semimetal polarization detectors with configurable polarity transition,” *Nat. Photonics* **15**(8), 614–621 (2021).
6. B. Yang, D. Ma, W. Liu, *et al.*, “Deep-learning-based colorimetric polarization-angle detection with metasurfaces,” *Optica* **9**(2), 217 (2022).
7. A. H. Dorrah, N. A. Rubin, A. Zaidi, *et al.*, “Metasurface optics for on-demand polarization transformations along the optical path,” *Nat. Photonics* **15**(4), 287–296 (2021).
8. L. Li, Y. Shuang, Q. Ma, *et al.*, “Intelligent metasurface imager and recognizer,” *Light: Sci. Appl.* **8**(1), 97 (2019).
9. F. Yang, H. I. Lin, M. Y. Shalaginov, *et al.*, “Reconfigurable Parfocal Zoom Metalens,” *Adv. Opt. Mater.* **10**(17), 2200721 (2022).
10. X. He, L. Deng, Y. Yang, *et al.*, “Multifunctional ultrathin reflective metasurface via polarization-decoupled phase for arbitrary circularly or elliptically polarized waves,” *Opt. Express* **29**(8), 12736–12749 (2021).
11. G. Cao, H.-X. Xu, L.-M. Zhou, *et al.*, “Infrared metasurface-enabled compact polarization nanodevices,” *Mater. Today (Oxford, U. K.)* **50**, 499–515 (2021).
12. Y. Intaravanne, R. Wang, H. Ahmed, *et al.*, “Color-selective three-dimensional polarization structures,” *Light: Sci. Appl.* **11**(1), 302 (2022).
13. A. H. Naqvi and S. Lim, “Hydrodynamic metasurface for programming electromagnetic beam scanning on the Azimuth and elevation planes,” *Microsyst. Nanoeng.* **8**(1), 43 (2022).
14. M. Liu, W. Zhu, P. Huo, *et al.*, “Multifunctional metasurfaces enabled by simultaneous and independent control of phase and amplitude for orthogonal polarization states,” *Light: Sci. Appl.* **10**(1), 107 (2021).
15. Q. D. Peixia Zheng, Z. Li, Z. Ye, *et al.*, “Metasurface-based key for computational imaging encryption,” *Sci. Adv.* **7**(21), 7 (2021).
16. M. Ossiander, M. L. Meretska, H. K. Hampel, *et al.*, “Extreme ultraviolet metalens by vacuum guiding,” *Science* **380**(6640), 59–63 (2023).
17. P.-Y. Hsieh, S.-L. Fang, Y.-S. Lin, *et al.*, “Integrated metasurfaces on silicon photonics for emission shaping and holographic projection,” *Nanophotonics* **11**(21), 4687–4695 (2022).
18. X. Zhao, G. Duan, A. Li, *et al.*, “Integrating microsystems with metamaterials towards metadevices,” *Microsyst. Nanoeng.* **5**(1), 5 (2019).
19. J. Jang, T. Badloe, and J. Rho, “Unlocking the future of optical security with metasurfaces,” *Light: Sci. Appl.* **10**(1), 144 (2021).
20. S. Klimmer, O. Ghaebi, Z. Gan, *et al.*, “All-optical polarization and amplitude modulation of second-harmonic generation in atomically thin semiconductors,” *Nat. Photonics* **15**(11), 837–842 (2021).
21. Y. Mu, M. Zheng, J. Qi, *et al.*, “A large field-of-view metasurface for complex-amplitude hologram breaking numerical aperture limitation,” *Nanophotonics* **9**(16), 4749–4759 (2020).

22. L. Zhu, C. T. Xu, P. Chen, *et al.*, “Pancharatnam-Berry phase reversal via opposite-chirality-coexisted superstructures,” *Light: Sci. Appl.* **11**(1), 135 (2022).
23. M. Rafayelyan, G. Tkachenko, and E. Brasselet, “Reflective Spin-Orbit Geometric Phase from Chiral Anisotropic Optical Media,” *Phys. Rev. Lett.* **116**(25), 253902 (2016).
24. C. Wan, Z. Li, S. Wan, *et al.*, “Electric-Driven Meta-Optic Dynamics for Simultaneous Near- Far-Field Multiplexing,” *Adv. Funct. Mater.* **32**, 6 (2022).
25. H. Gao, X. Fan, Y. Wang, *et al.*, “Multi-foci metalens for spectra and polarization ellipticity recognition and reconstruction,” *Opto-Electron. Sci.* **2**(3), 220026 (2023).
26. N. Yu, P. Genevet, M. A. Kats, *et al.*, “Light Propagation with Phase Discontinuities: Generalized Laws of Reflection and Refraction,” *Science* **334**(6054), 333–337 (2011).
27. H.-S. Ee and R. Agarwal, “Tunable Metasurface and Flat Optical Zoom Lens on a Stretchable Substrate,” *Nano Lett.* **16**(4), 2818–2823 (2016).
28. S. M. Kamali, E. Arbabi, A. Arbabi, *et al.*, “Highly tunable elastic dielectric metasurface lenses,” *Laser Photonics Rev.* **10**(6), 1002–1008 (2016).
29. M. A. Shameli and L. Yousefi, “Absorption enhancement in thin-film solar cells using an integrated metasurface lens,” *J. Opt. Soc. Am. B* **35**(2), 223 (2018).
30. H. Ahmed, M. A. Ansari, Y. Li, *et al.*, “Dynamic control of hybrid grafted perfect vector vortex beams,” *Nat. Commun.* **14**(1), 3915 (2023).
31. B. Wang, W. Liu, M. Zhao, *et al.*, “Generating optical vortex beams by momentum-space polarization vortices centred at bound states in the continuum,” *Nat. Photonics* **14**(10), 623–628 (2020).
32. G. Xue, Q. Zhai, H. Lu, *et al.*, “Polarized holographic lithography system for high-uniformity microscale patterning with periodic tunability,” *Microsyst. Nanoeng.* **7**(1), 31 (2021).
33. X. Zhang, S. Yang, W. Yue, *et al.*, “Direct polarization measurement using a multiplexed Pancharatnam–Berry metahologram,” *Optica* **6**(9), 1190 (2019).
34. G. Qu, W. Yang, Q. Song, *et al.*, “Reprogrammable meta-hologram for optical encryption,” *Nat. Commun.* **11**(1), 5484 (2020).
35. X. Zhang, J. Jin, M. Pu, *et al.*, “Ultrahigh-capacity dynamic holographic displays via anisotropic nanoholes,” *Nanoscale* **9**(4), 1409–1415 (2017).
36. X. Li, R. Zhao, Q. Wei, *et al.*, “Code Division Multiplexing Inspired Dynamic Metasurface Holography,” *Adv. Funct. Mater.* **31**, 6 (2021).
37. Y. Jia, C. Qian, Z. Fan, *et al.*, “A knowledge-inherited learning for intelligent metasurface design and assembly,” *Light: Sci. Appl.* **12**(1), 82 (2023).
38. J. Xiong, J. Shen, Y. Gao, *et al.*, “Real-Time On-Demand Design of Circuit-Analog Plasmonic Stack Metamaterials by Divide-and-Conquer Deep Learning,” *Laser Photonics Rev.* **17**, 2100738 (2023).
39. Z. Wang, Y. Xiao, K. Liao, *et al.*, “Metasurface on integrated photonic platform: from mode converters to machine learning,” *Nanophotonics* **11**(16), 3531–3546 (2022).
40. X. Luo, Y. Hu, X. Ou, *et al.*, “Metasurface-enabled on-chip multiplexed diffractive neural networks in the visible,” *Light: Sci. Appl.* **11**(1), 158 (2022).
41. S. Zhang, L. Huang, G. Geng, *et al.*, “Full-Stokes polarization transformations and time sequence metasurface holographic display,” *Photonics Res.* **10**(4), 1031 (2022).
42. D. Lee, M. Go, M. Kim, *et al.*, “Multiple-patterning colloidal lithography-implemented scalable manufacturing of heat-tolerant titanium nitride broadband absorbers in the visible to near-infrared,” *Microsyst. Nanoeng.* **7**(1), 14 (2021).
43. H. H. Li, “Refractive index of alkaline earth halides and its wavelength and temperature derivatives,” *J. Phys. Chem. Ref. Data* **9**(1), 161–290 (1980).
44. E. D. Palik, *Handbook of Optical Constants of Solids* (Academic Press, 1985).
45. J. Sisler, W. T. Chen, A. Y. Zhu, *et al.*, “Controlling dispersion in multifunctional metasurfaces,” *APL Photonics* **5**(5), 056107 (2020).
46. W. T. Chen, A. Y. Zhu, V. Sanjeev, *et al.*, “A broadband achromatic metalens for focusing and imaging in the visible,” *Nat. Nanotechnol.* **13**(3), 220–226 (2018).
47. S. W. D. Lim, M. L. Meretska, and F. Capasso, “A High Aspect Ratio Inverse-Designed Holey Metalens,” *Nano Lett.* **21**(20), 8642–8649 (2021).
48. R. Barboza, U. Bortolozzo, M. G. Clerc, *et al.*, “Berry Phase of Light under Bragg Reflection by Chiral Liquid-Crystal Media,” *Phys. Rev. Lett.* **117**(5), 053903 (2016).
49. Y. Bao, L. Wen, Q. Chen, *et al.*, “Toward the capacity limit of 2D planar Jones matrix with a single-layer metasurface,” *Sci. Adv.* **7**(25), 6 (2021).
50. K. Huang, J. Deng, H. S. Leong, *et al.*, “Ultraviolet Metasurfaces of 80 Efficiency with Antiferromagnetic Resonances,” *Laser Photonics Rev.* **13**, 9 (2019).
51. Y. Ren, S. Guo, W. Zhu, *et al.*, “Full-Stokes Polarimetry for Visible Light Enabled by an All-Dielectric Metasurface,” *Adv. Photonics Res.* **3**, 8 (2022).